ACS OMEGA

http://pubs.acs.org/journal/acsodf

Article

Effect of the Structure of Highly Porous Silica Extracted from Sugarcane Bagasse Fly Ash on Aflatoxin B1 Adsorption

Sirada Sungsinchai, Chalida Niamnuy,* Sakamon Devahastin, Xiao Dong Chen, and Metta Chareonpanich

Cite This: *ACS Omega* 2023, 8, 19320−19328

Read Online

ACCESS | Metrics & More | Article Recommendations

ABSTRACT: Sugarcane bagasse fly ash is industrial waste produced by incinerating biomass to generate power and steam. The fly ash contains SiO_2 and Al_2O_3, which can be used to prepare aluminosilicate. This latter material exhibits high potential as an adsorbent in various applications, including the livestock industry where issues related to contamination of aflatoxins in animal feeds need to be addressed; addition of adsorbents can help decrease the concentration of aflatoxins during feed digestion. In this study, the effect of the structure of silica prepared from sugarcane bagasse fly ash on physicochemical properties and aflatoxin B1 (AFB1) adsorption capability compared with that of bentonite was investigated. BPS-5, Xerogel-5, MCM-41, and SBA-15 mesoporous silica supports were synthesized using sodium silicate hydrate (Na_2SiO_3) from sugarcane bagasse fly ash as a silica source. BPS-5, Xerogel-5, MCM-41, and SBA-15 exhibited amorphous structures, while sodium silicate possessed a crystalline structure. BPS-5 possessed larger pore size, pore volume, and pore size distribution with a bimodal mesoporous structure, while Xerogel-5 exhibited lower pore size and pore size distribution with a unimodal mesoporous structure. BPS-5 with a negatively charged surface exhibited the highest AFB1 adsorption capability compared with other porous silica. However, the AFB1 adsorption capability of bentonite was superior to those of all porous silica. Sufficient pore diameter with high total pore volume as well as high intensity of acid sites and negative charge on the surface of the adsorbent is required to increase AFB1 adsorption in the in vitro gastrointestinal tract of animals.

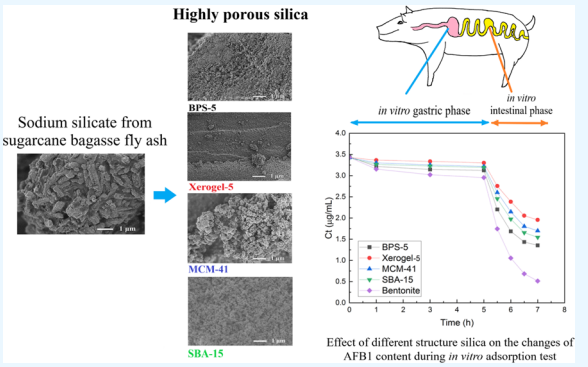

Effect of different structure silica on the changes of AFB1 content during *in vitro* adsorption test

1. INTRODUCTION

Sugarcane bagasse fly ash is produced in large tonnage in sugar and ethanol plants where the bagasse is incinerated to generate power and steam; the fly ash is indeed produced due to the incomplete incineration of the bagasse.[1] Such fly ash has been reported to cause serious environmental problems, leading to much concern and banning against its direct utilization.[2,3] Finding a means to turn this industrial waste into a valuable product is therefore of much interest. Since bagasse fly ash is composed of unburned carbon, SiO_2, and Al_2O_3, using environmentally accepted methods to convert the fly ash into useful mesoporous silica templates is highly plausible.[1,3] Several researchers have indeed proposed the synthesis of mesoporous silica materials such as MCM-41 and SBA-15 from fly ash via a basic medium.[1,3] Mesoporous silica can then be used in such industrial applications as catalysts, catalyst support materials, additives in cement and concrete, and adsorbents.[4,5] Of particular interest is the use of mesoporous silica as an adsorbent in the removal of mycotoxins from human foods and animal feeds.

Mycotoxins are toxic metabolic compounds produced by some molds. The most common mycotoxin of concern to humans and livestock is aflatoxin.[6] The toxin is indeed one of the most dangerous contaminants that can be present in human foods and animal feeds.[7] Among the many aflatoxins that can be found, aflatoxin B1 (AFB1) is well known for its toxicity and occurrence in animal feeds.[8] Activated carbon, hydrated sodium calcium aluminosilicate, dietary clay, zeolites, and bentonite[7,9] as well as silica are most commonly used as commercial adsorbents to remove AFB1 from human foods and animal feeds, as these materials possess large pore volumes and high surface areas. The use of zeolites and hydrated sodium calcium aluminosilicate may, however, result in the release of toxic components, including heavy metals or dioxins.[10] On the other hand, activated carbon, which is one of the most popular adsorbents due to its low cost, possesses excessively fine pore characteristics that may limit the transport

Received: December 31, 2022
Accepted: May 15, 2023
Published: May 25, 2023

https://doi.org/10.1021/acsomega.2c08299
ACS Omega 2023, 8, 19320−19328

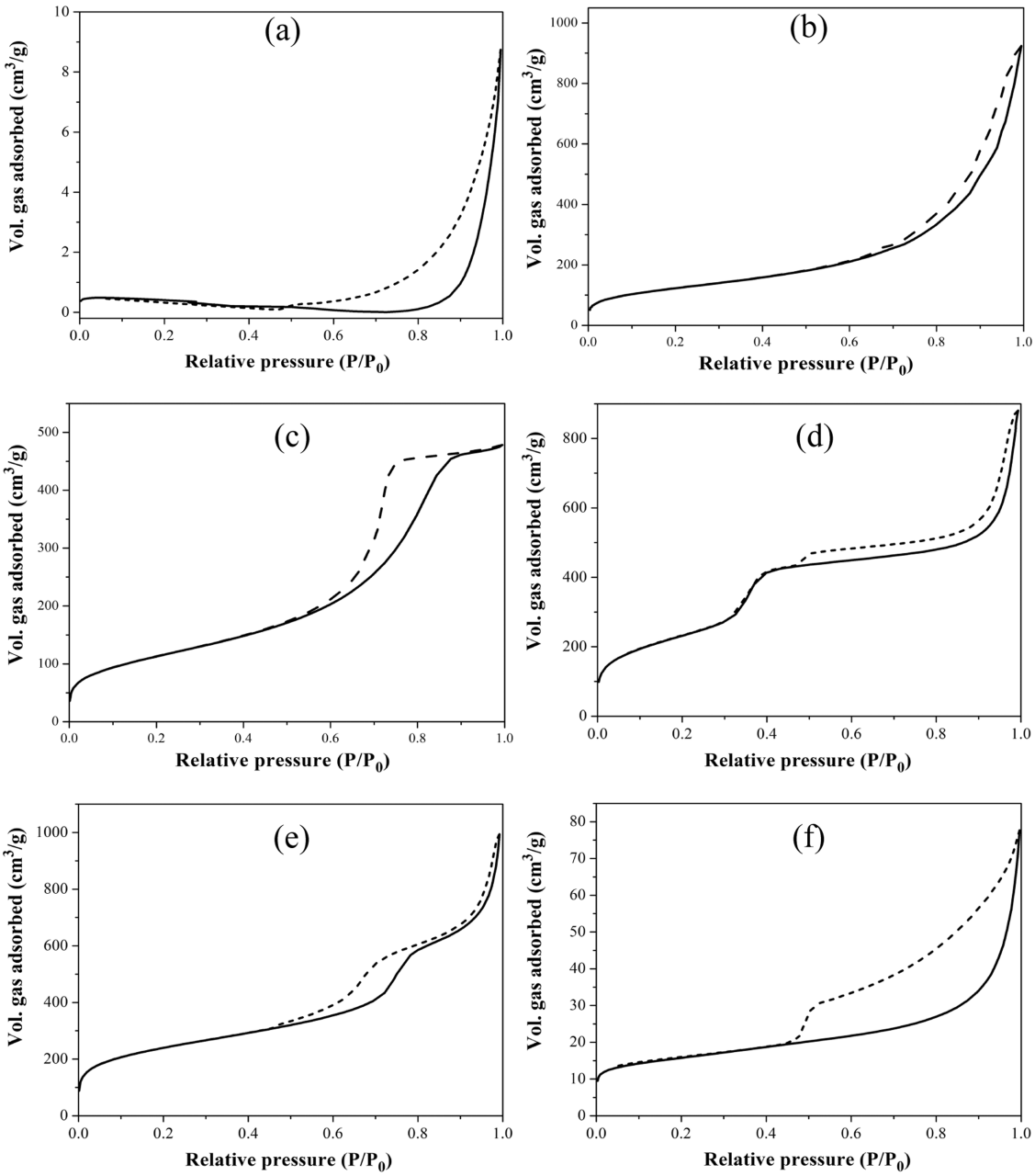

Figure 1. Nitrogen sorption isotherms of (a) sodium silicate, (b) BPS-5, (c) Xerogel-5, (d) MCM-41, (e) SBA-15, and (f) bentonite. Legends: — adsorption; – – – desorption.

of the larger molecules of AFB1 into the pores.[11] Selection of a suitable adsorbent material remains a challenge for AFB1.

Mesoporous silica has attracted considerable attention due to its higher surface area, ordered porosity, narrow pore size distribution, high thermal stability, and ease of synthesis from various agricultural wastes. In particular, there is no evidence of its toxicity after oral intake.[12,13] Several studies have reported that silica and silica-based adsorbents exhibit high effectiveness in adsorbing mycotoxin.[14−17] Li et al.[13] studied the synthesis of mesoporous silica (MCM-41) from rice husk and used it to adsorb AFB1 from peanut oil. Such MCM-41 exhibited high specific surface area, pore volume, and narrow pore size distribution. Its AFB1 adsorption capability was comparable to that of commercial natural montmorillonite and activated carbon. Pellicer-Castell et al.[18] studied the use of mesoporous silica (UVM-7) as an SPE sorbent for the extraction of aflatoxin M1 (AFM1) from milk and yogurt. The high AFM1 adsorption ability of UVM-7 was noted in both cases of milk and yogurt. The repeatability of the sorbent was also proved. AFM1 removal capabilities of the UVM-7 sorbent were comparable to that obtained using a reference protocol for milk and yogurt clean-up. While previous studies have shown that mesoporous silica is highly efficient for AFB1 absorption,[13] there is so far no study that investigates the use of different mesoporous silica such as BPS-5, Xerogel-5, MCM-41, and SBA-15 and the effects of their surface characteristics, porosity, and size distributions on mycotoxin, especially, AFB1 adsorption capability. This missing information is of much importance, as it can be used as a guideline to develop a silica-based adsorbent, especially the one from such agricultural wastes as sugarcane bagasse fly ash, in the future.

https://doi.org/10.1021/acsomega.2c08299
ACS Omega 2023, 8, 19320−19328

Based on the aforementioned arguments, the objective of the present study was to investigate the use of sugarcane bagasse fly ash as a source of silica to produce highly porous silica in various forms. The study also investigated selected key physicochemical properties of the silica adsorbents and examined their effectiveness in AFB1 adsorption.

2. RESULTS AND DISCUSSION

2.1. Specific Surface Area and Pore Size Distribution.

The adsorption−desorption isotherms of sodium silicate, highly porous silica, and bentonite are shown in Figure 1. Since capillary condensation occurs in mesopores, the desorption path would expectedly be different from the adsorption path, resulting in the formation of a hysteresis loop.[19] BPS-5 (Figure 1b) exhibited a composite isotherm between type IV and type II, which implies the existence of mesopore and macropore structures.[20] A type between type IV and type II isotherms with a hysteresis loop was observed in the case of sodium silicate (Figure 1a). Xerogel-5, MCM-41, and SBA-15 (Figure 1c−e) as well as bentonite (Figure 1f) exhibited type IV isotherms with a hysteresis loop, indicating the existence of a mesopore structure.[20,21]

The type of hysteresis loop is mostly associated with the pore shape. In the present study, straight-pore and sinusoidal-pore structures with monomodal and bimodal pore sizes were classified as highly porous silica. BPS-5 and Xerogel-5 had sinusoidal-pore silica with monomodal and bimodal pore sizes, respectively. This is because the pore structures of BPS-5 and Xerogel-5 were formed by the aggregation of silica nanoparticles, resulting in an interconnected wormhole structure.[20] MCM-41 and SBA-15 exhibited straight-pore silica, as CTAC and Pluronic P123 are, respectively, used as the templates. However, the straight pores of MCM-41 and SBA-15 are obtained as a result of template removal after calcination.[20]

Figure 2 shows the pore size distribution of sodium silicate, highly porous silica, and bentonite. Sodium silicate exhibited

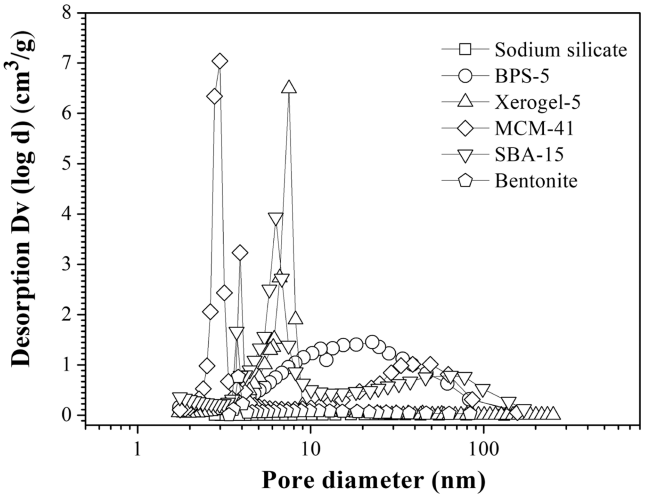

Figure 2. Pore size distribution of sodium silicate, BPS-5, Xerogel-5, MCM-41, SBA-15, and bentonite.

broad monomodal pore sizes of 57.23 nm, while bentonite possessed narrow monomodal pore sizes of 9.17 nm. These results correspond to the average pore diameters of sodium silicate and bentonite, as shown in Table 1. BPS-5 exhibited a broad pore distribution, with bimodal mesoporous sizes of

Table 1. Physical Properties of Highly Porous Silica and Bentonite

sample	BET surface area (m^2/g)	pore diameter (nm)	average pore diameter (nm)	pore volume (cm^3/g) small pore	pore volume (cm^3/g) large pore
sodium silicate	0.95	57.23	57.23	0.014	
		Highly Porous Silica			
BPS-5	439.35	11.43, 22.70	13.05	1.00	1.56
Xerogel-5	408.95	7.25	7.25	0.74	
MCM-41	848.76	3.00−3.91, 44.04	6.43	1.01	0.29
SBA-15	825.36	7.47	7.47	1.54	
bentonite	52.18	9.17	9.17	0.12	

11.43 and 22.70 nm; the results are ascribed to the nature of the chitosan template at a relatively high pH value.[22] However, Xerogel-5 and SBA-15 presented narrow monomodal pore sizes of 7.25 and 7.47 nm, respectively; the results also correspond to the average pore diameters shown in Table 1. The sharp and narrow pore size distributions of Xerogel-5, MCM-41, SBA-15, and bentonite indicate uniform pore sizes and structures.[20] However, MCM-41 exhibited bimodal pores, with smaller and larger pore sizes of 3.00−3.91 and 44.04 nm, respectively.

The physical properties of sodium silicate and highly porous silica are given in Table 1. Sodium silicate exhibited the lowest surface area (0.95 m^2/g) and pore volume (0.014 cm^3/g). This is due to the fact that sodium silicate displayed a monomodal pore size, with the largest pore diameter of 57.23 nm, which corresponds to a macropore structure (pore diameter >50 nm).[23]

The surface area and pore volume of all of the highly porous silica significantly increased, while the average pore diameter significantly decreased after being synthesized from sodium silicate. Additionally, all of the highly porous silica exhibited higher surface areas compared with bentonite. This indicates that sodium silicate prepared from bagasse fly ash can produce highly porous silica. MCM-41, in particular, exhibited the highest surface area and had 1.93, 2.08, 1.03, and 16.27 times larger surface area than BPS-5, Xerogel-5, SBA-15, and bentonite, respectively. This is ascribed to the fact that MCM-41 possessed bimodal pore sizes, with smaller and larger pore diameters of 3.00−3.91 and 44.04 nm, respectively; its average pore diameter was 6.43 nm.

2.2. Crystalline Structure. The crystalline structures of sodium silicate and highly porous silica are shown in Figure 3. The small-angle X-ray scattering (SAXS) pattern of sodium silicate (Figure 3A(a)) shows a similar diffraction peak with that of SiO_2,[24] indicating that bagasse fly ash can produce sodium silicate. BPS-5, Xerogel-5, MCM-41, and SBA-15, as shown in Figure 3A(b−e), possessed similar peak characteristics; the results agree with those of Tanggarnjanavalukul et al.[20] In the case of BPS-5 and Xerogel-5, the smaller peaks disappeared, while the major peaks shifted to smaller 2θ, and the peak intensity significantly reduced, indicating a disordered hexagonal structure with larger pore sizes.[20] These correspond to the results shown in Figure 2 and Table 1. In the case of MCM-41 (Figure 3A(d)), peak intensity was observed at a 2θ of 2.4°, corresponding to the reflection plane (100), while smaller peaks at 2θ of 3.8 and 4.5° corresponded to the two

https://doi.org/10.1021/acsomega.2c08299
ACS Omega 2023, 8, 19320−19328

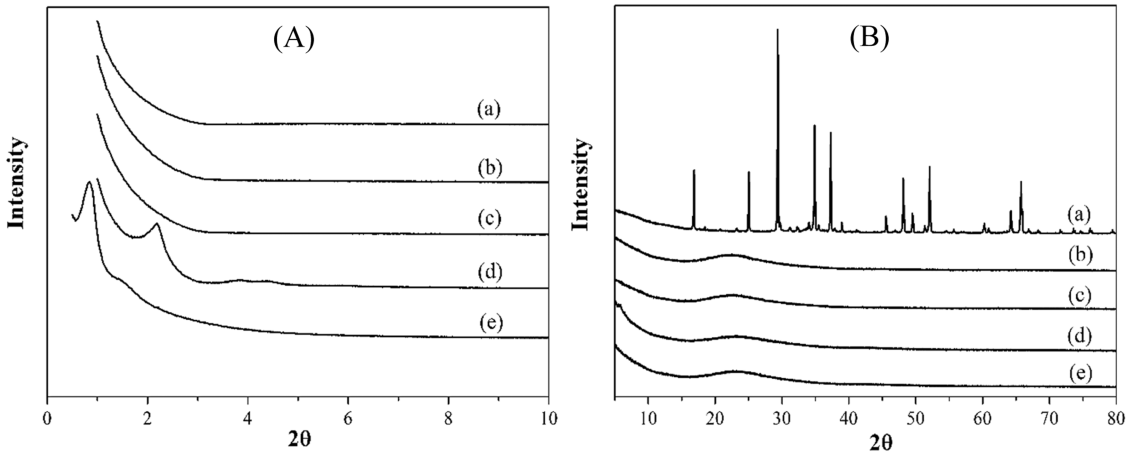

Figure 3. (A) Small-angle X-ray scattering and (B) XRD patterns of (a) sodium silicate and highly porous silica, (b) BPS-5, (c) Xerogel-5, (d) MCM-41, and (e) SBA-15.

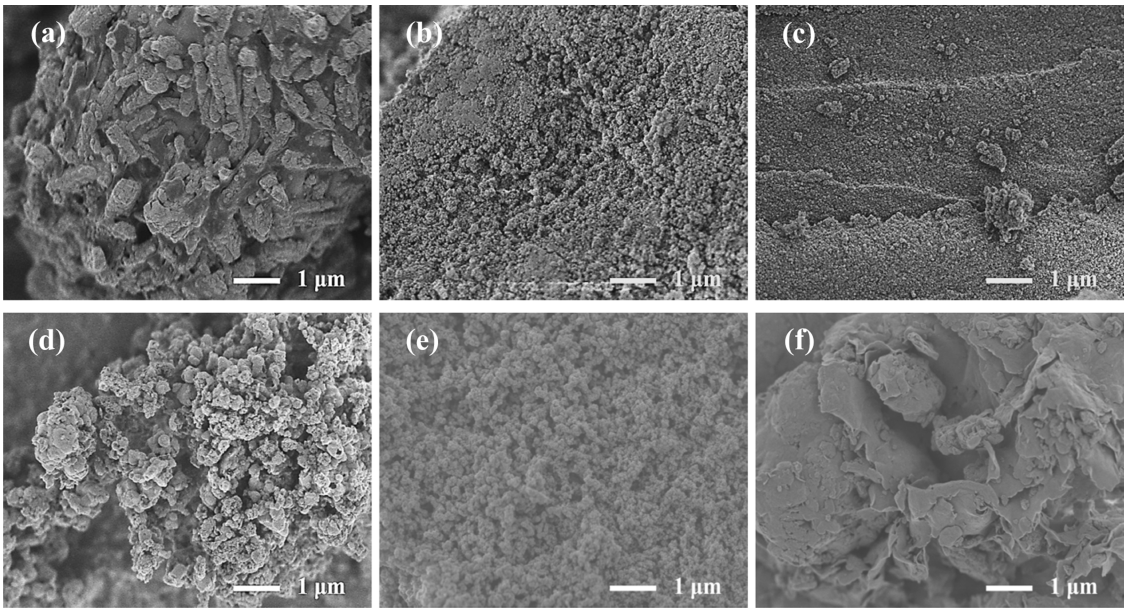

Figure 4. FESEM images of (a) sodium silicate, (b) BPS-5, (c) Xerogel-5, (d) MCM-41, (e) SBA-15, and (f) bentonite.

reflections planes (110) and (200), respectively. This clearly indicates a long-range, ordered, hexagonal, mesoporous structure, similar to the MCM-41 structure reported by Kiatphuengporn et al.[25] SBA-15 exhibited a well-ordered 2D hexagonal mesoporous structure (Figure 3A(e)), as confirmed by the diffraction peaks at 2θ of 0.8, 1.6, and 1.8°, which corresponded to the reflection planes (100), (110), and (200), respectively.[20]

Figure 3B(a) shows the crystalline structure of sodium silicate derived from bagasse fly ash after calcination. The crystalline peaks were in the 2θ range of 16.84−65.73°, with the highest intensity peak at 29.38°; the results are similar to those reported by Siregar et al.[5] On the other hand, BPS-5, Xerogel-5, MCM-41, and SBA-15 (Figure 3B) exhibited strong broad peaks at 2θ of around 15−25°, indicating that they are amorphous silica.[26] The *d*-spacing, or atomic resolution, is the distance between adjacent lattice plans. The *d*-spacing values were 4.27, 4.18, 4.10, and 4.12 Å for BPS-5, Xerogel-5, MCM-41, and SBA-15, respectively.

2.3. Morphology. Morphologies of sodium silicate, highly porous silica, and bentonite are shown in Figure 4. Agglomeration and partially fused particles can be seen in the microstructure of sodium silicate (Figure 4a). This is due to the lower specific surface area, pore size, and pore volume of sodium silicate compared with other highly porous silica and bentonite as mentioned earlier. Porous characteristics were observed in all highly porous silica. BPS-5 (Figure 4b) showed a non-uniformly distributed structure, which was different from the structural uniformity of Xerogel-5 (Figure 4c), although their specific surface areas were very similar. These results correspond to the bimodal mesoporous structure of BPS-5 mentioned earlier. MCM-41 (Figure 4d) also possessed agglomerated particle characteristics, which correspond to the bimodal mesoporous structures with smaller and larger pores, as shown in Figure 2 and Table 1. SBA-15 (Figure 4e), on the other hand, revealed a uniform structure with smaller particle sizes compared with other samples; this was confirmed by the narrow monomodal pore size distribution (Figure 2) and high specific surface area (Table 1). Bentonite (Figure 4f)

https://doi.org/10.1021/acsomega.2c08299
ACS Omega 2023, 8, 19320−19328

was composed of individual varying-size platelets, which conglomerated into large-size particles.[27] Such characteristics correspond to the lowest specific surface area compared with those of other samples, as shown in Table 1.

2.4. FTIR Spectra. Functional groups of sodium silicate, highly porous silica, and bentonite are shown in Figure 5. The

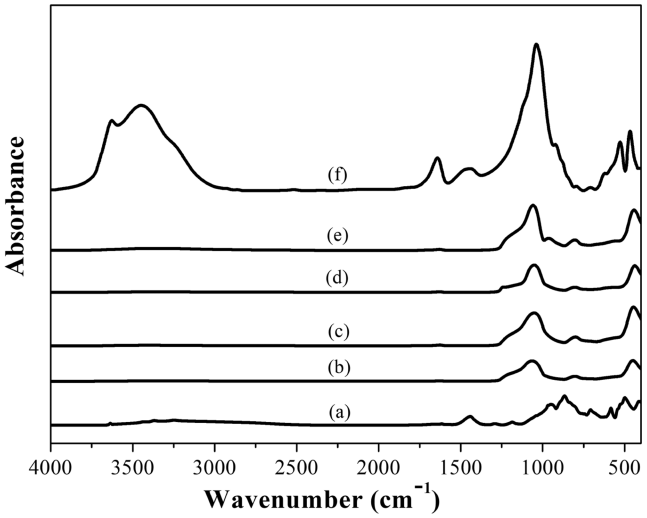

Figure 5. FTIR spectra of (a) sodium silicate, (b) BPS-5, (c) Xerogel-5, (d) MCM-41, (e) SBA-15, and (f) bentonite.

characteristic bands of sodium silicate (Figure 5a) for the silanol OH group and adsorbed water are at 3249−3369 cm^{-1}, while the broad bands at 951−1441 and 500−866 cm^{-1} correspond to the Si−O−Si and Al−O−Si bond groups, respectively.[2] BPS-5, Xerogel-5, MCM-41, and SBA-15 exhibited spectra in the range of 600−1400 cm^{-1} (Figure 5b−e), which are mostly the framework vibration characteristics of the tetrahedron of silica with oxygen.[28−30] Additionally, peak intensities at 820 and 1090 cm^{-1} were clearly observed in all of the highly porous silica. This is due to the symmetric and asymmetric stretch vibrations of Si−O−Si bonds (siloxane group), implying that these material structures can be ascribed to the composite Si−O stretching in silica.[30] Furthermore, the peaks of BPS-5, Xerogel-5, and MCM-41 at 3000−3700 cm^{-1} (hydroxyl stretching) and 1640 cm^{-1} (bending vibration of the free hydroxyl group) disappeared compared with the spectrum of sodium silicate. This is due to the stretching mode of broken Si−O bridges, which corresponds to the formation mode of Si−O−Si in bimodal mesoporous silica.[30] These results indicate that BPS-5, Xerogel-5, MCM-41, and SBA-15 had been prepared from sodium silicate to form a bimodal mesoporous material; the results are in agreement with those provided by the XRD patterns.[30] In the case of bentonite, the peaks at 3627 and 3448 cm^{-1} correspond to the interlayer and intralayer H-bonded O−H stretching, respectively.[31] A peak at 1642 cm^{-1} indicates the bending vibration of water (H−O−H).[32] The peak at 940 cm^{-1} corresponds to the bending vibration of Al−Al−OH, while the peak at 630 cm^{-1} is identified as belonging to the vibration of Al−OH.[31,32] The bands at 528 and 470 cm^{-1} are due to the bending vibrations of Al−O−Si and Si−O−Si, respectively.[32]

Figure 6 shows the NH_3-TPD profiles of the synthesized silica and bentonite. The NH_3 desorption peaks were distributed in the ranges of 100−200 °C (weak acid sites)

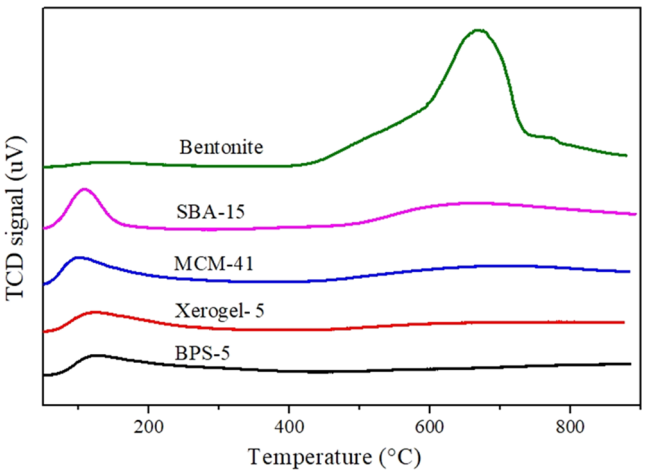

Figure 6. NH_3-TPD profiles of highly porous silica and bentonite.

and 400−800 °C (strong acid sites).[33] All of the synthesized porous silica only showed the intensities of the weak acid sites. SBA-15 demonstrated the highest intensity of the weak acid sites. Bentonite presented the intensity of only the strong acid sites and clearly had the highest intensity of acid sites compared with all of the synthesized silica.

Table 2 lists the ζ potentials of silica and bentonite. ζ Potential is the electrokinetic potential in a colloidal system

Table 2. ζ Potentials of Highly Porous Silica and Bentonite

	ζ Potential (mV)				
pH	BPS-5	Xerogel-5	MCM-41	SBA-15	Bentonite
2.5	−15.52	−18.72	−15.89	−12.90	−31.50
6.5	−32.74	−31.49	−31.94	−31.85	−41.82

and can be used to characterize surface charged particles. It was noted here that the pH of a medium altered the ζ potential and that all of the samples exhibited negatively charged surfaces. ζ Potentials of all of the highly porous silica were similar at pH 2.5 and 6.5. Bentonite exhibited the highest negatively charged surface at both pH 2.5 and 6.5.

2.5. In Vitro AFB1 Adsorption Capability. In vitro AFB1 adsorption capacities of the highly porous silica and bentonite are shown in Table 3. AFB1 adsorption increased with an increase in the in vitro digestion time. BPS-5 exhibited the highest AFB1 adsorption at 5 h (after gastric phase) and 7 h (after intestinal phase) of the in vitro digestion compared with the other silica. These results correspond to the larger pore sizes and pore volume of BPS-5, although it possessed a smaller surface area than MCM-41 and SBA-15. Xerogel-5 exhibited the lowest AFB1 adsorption. This is because of the smaller pore sizes and pore volume of Xerogel-5, although it exhibited a comparable surface area to BPS-5. These results indicate that adequately large pore sizes are necessary for AFB1 adsorption, although the molecular size of AFB1 is only around 1 nm.[7]

Bentonite showed higher AFB1 adsorption capability than the synthesized silica, although the former had a smaller surface area. This is because of the high intensity of the surface acid sites[33] and the highly negatively charged surface of bentonite.[34]

2.6. AFB1 Adsorption Kinetics. Figure 7 shows the changes in AFB1 concentration during in vitro digestion. It is

https://doi.org/10.1021/acsomega.2c08299
ACS Omega 2023, 8, 19320−19328

Table 3. In Vitro AFB1 Adsorption Capacities of Highly Porous Silica and Bentonite[a]

	adsorption (%)				
digestion phase	BPS-5	Xerogel-5	MCM-41	SBA-15	bentonite
after gastric phase	9.32 ± 0.65[c]	3.71 ± 0.12[a]	6.07 ± 0.41[b]	6.25 ± 0.39[b]	17.08 ± 0.98[d]
after intestinal phase	60.68 ± 3.11[c]	42.97 ± 2.24[a]	50.38 ± 3.03[b]	54.77 ± 2.27[bc]	84.98 ± 3.60[d]

[a]Values in the same row with different superscript letters are significantly different ($p < 0.05$).

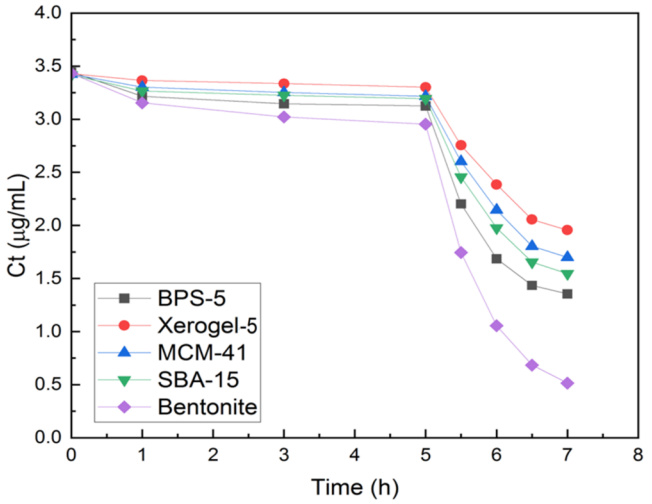

Figure 7. Concentrations of AFB1 during in vitro digestion: gastric phase (0−5 h) and intestinal phase (5−7 h).

seen that the reduction in AFB1 during the gastric phase was in all cases limited. Higher adsorption rates can be seen during the intestinal phase.[35] This corresponds to the fact that the negatively charged surfaces of silica and bentonite at pH 6.5 were significantly higher than those at pH 2.5.[34]

AFB1 adsorption kinetics of the highly porous silica during the intestinal phase are shown in Figure 8. The pseudo-first-order kinetic model was noted to best represent the experimental data. Similar observations were noted in the other studies on mycotoxin adsorption kinetics.[13,36,37]

The values of the correlation coefficient (R^2), first-order rate constant (k_a), and concentration of AFB1 adsorbed at equilibrium (q_e) are given in Table 4. The R^2, k_a, and q_e values were in the ranges of 0.9610−0.9863, 0.95−1.74 (h^{-1}), and 1.75−3.03 (mg/g), respectively. The results indicated that BPS-5 provided the highest k_a (1.70 h^{-1}) and q_e (2.17 mg/g) compared with the values belonging to the other highly porous silica. This is due to the largest pore diameters with higher surface area and acid sites on the surface of BPS-5. Such characteristics in turn resulted in the highest adsorption capability of AFB1 during in vitro intestinal digestion (pH 6.5). Additionally, the observed adsorption behavior of BPS-5 could be ascribed to the characteristic bimodal mesoporous sizes and volumes (Table 1), which helped enhance the diffusion of the AFB1 molecules from the surface into the pores (pore diffusion).[37] Compared with the previously reported results, the ability of our highly porous silica, especially BPS-5 (0.607 mg/g), in adsorbing AFB1 was higher than those of magnetic mesoporous silica (0.165 mg/g),[38] magnetic graphene oxide (2.36×10^{-6} mg/g),[36] natural montmorillonite (0.166 mg/g),[13] rice husk-based mesoporous silica (0.189 mg/g),[13] and commercial activated carbon (0.200 mg/g).[13]

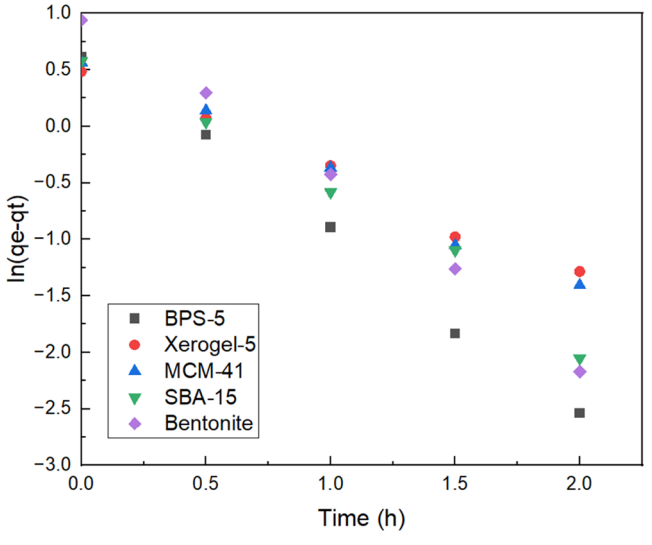

Figure 8. Pseudo-first-order kinetic plots for adsorption of AFB1 during in vitro intestinal digestion.

Table 4. Pseudo-First-Order Adsorption Parameters (R^2, k_a, and q_e) for Adsorption of AFB1 into Highly Porous Silica and Bentonite during In Vitro Intestinal Digestion

	pseudo-first-order kinetic model		
sample	R^2	k_a (h^{-1})	q_e (mg/g)
BPS-5	0.9815	1.70	2.17
Xerogel-5	0.9610	0.95	1.75
MCM-41	0.9707	1.07	1.97
SBA-15	0.9698	1.28	2.00
bentonite	0.9863	1.74	3.03

The adsorption rates of all of the highly porous silica during in vitro intestinal digestion were nevertheless lower than that of bentonite. This is due to the fact that the hydroxyl group of bentonite (see Figure 5) played an important role in the bonding of AFB1 through H-bonding during in vitro digestion.[36] In the cases of the highly porous silica, the lower negative charges, as shown in Table 2, resulted in the lower attractive forces between the silica surfaces and AFB1 molecules. This in turn resulted in the observed lower adsorption rates.[14]

3. CONCLUSIONS

Sodium silicate derived from sugarcane bagasse fly ash has proved to have high potential for the synthesis of highly porous silica with monomodal and bimodal porous structures; these results were confirmed by both the XRD patterns and FTIR spectra. Specific surface areas, pore sizes, and pore volumes of the synthesized highly porous silica were larger, while the portions of the crystalline structure were smaller than those of bagasse fly ash-derived sodium silicate and other porous silica;

https://doi.org/10.1021/acsomega.2c08299
ACS Omega 2023, 8, 19320−19328

the results are in good agreement with the results on AFB1 adsorption. BPS-5 showed the highest AFB1 adsorption capability compared with other porous silica. Bentonite nevertheless exhibited significantly higher AFB1 adsorption capability than all of the synthesized porous silica. Extensive hydrogen bonding, suitable pore size diameter, and surface area as well as high-intensity acid sites and negatively charged surface of the adsorbent resulted in the higher capability of AFB1 adsorption. To improve the efficiency of the highly porous silica, further studies are necessary to evaluate the ability of various hybrid composite silica-based adsorbents on AFB1 adsorption in animal feed using both in vitro and in vivo digestion tests.

4. EXPERIMENTAL SECTION

4.1. Preparation of Sodium Silicate from Bagasse Fly Ash. Preparation of sodium silicate from bagasse fly ash was performed as per the modified methods of Ruengrung et al.[11] 18.648 g of bagasse fly ash (74.23% SiO_2) was mixed with 22.601 g of sodium carbonate (Na_2CO_3, Kemaus, NSW, Australia) for 30 min. After calcining at 850 °C for 1 h, using a heating rate of 10 °C/min, a blue solid product was obtained. 120 mL of deionized (DI) water was added to the product; the mixture was centrifuged at 8900 rpm for 10 min. The supernatant (green solution) was dried at 150 °C for 24 h and calcined at 850 °C for 1 h until sodium silicate was obtained.

4.2. Preparation of Highly Porous Silica. Highly porous silica, including BPS-5, Xerogel-5, MCM-41, and SBA-15, were synthesized by the methods outlined in the following subsections.

4.2.1. BPS-5 (Bimodal Porous Silica-5) Synthesis.[20] 0.4 g of chitosan was dissolved in 100 mL of acetic acid solution (1% v/v) at 40 °C for 30 min. Sodium silicate solution (Na_2SiO_3: 4.55 wt % SiO_2) was prepared from 3.52 g of sodium silicate powder dissolved in 3.74 g of DI water. Then, 10 mL of DI water was added. This sodium silicate solution was then instilled into the chitosan solution under continuous stirring at 40 °C. The pH value of the mixture was adjusted to 5 using 2 M HCl and 2 M NaOH solutions; stirring continued for 3 h at 40 °C. The obtained gel was transferred to a Teflon-lined autoclave and aged at 100 °C for 24 h, filtered, washed with DI water, and dried at 100 °C for 24 h. The final solid product was calcined at 600 °C for 4 h; the heating rate was 2 °C/min. The product was mashed to a size range of 53−106 μm and kept at room temperature until further analysis.

4.2.2. Xerogel-5 (Monomodal Porous Silica) Synthesis.[20] Sodium silicate solution was first prepared from 2.37 g of sodium silicate powder and 2.52 g of DI water. Then, 10 mL of DI water was added to the mixture. Subsequently, this sodium silicate solution was dropped into 100 mL of acetic acid in DI water (1% v/v) under stirring. 1 M HCl and 1 M NaOH solutions were added to the mixture under continuous stirring at 40 °C to adjust the pH to 5. After 3 h, the obtained gel was transferred to a Teflon-lined autoclave and then aged, washed, dried, and calcined in a similar way to that performed to prepare BPS-5. The final solid product was again mashed to a size range of 53−106 μm.

4.2.3. MCM-41 (Mesoporous Silica) Synthesis.[25] 25.287 g of cetyltrimethylammonium chloride (CTAC) was dissolved in 40 mL of DI water. 9.39 g of sodium silicate powder was dissolved in 9.97 g of DI water; 40 mL of DI water was then added. This sodium silicate solution was dropped into the CTAC solution under stirring. The pH was adjusted to 6.5 using 1 M sulfuric acid solution; the mixture was continuously stirred for 5 h. The pH was then adjusted to 11.25 using 1 M NaOH solution; stirring continued for 1 h. The obtained gel was transferred to a Teflon-lined autoclave, aged at 100 °C for 24 h, then filtered, and washed with DI water. The sample was dried at 100 °C for 24 h and then calcined at 550 °C for 4 h; a heating rate of 5 °C/min was used. The final solid product was again mashed to a size range of 53−106 μm.

4.2.4. SBA-15 (Mesoporous Silica) Synthesis.[20] 0.845 g of Pluronic P123 was dissolved in 60 mL of DI water overnight. 2.00 g of sodium silicate powder was dissolved in 2.12 g of DI water and then dropped into the Pluronic P123 solution. 5.4 mL of HCl (37 wt %) was added to the mixture; the content was stirred at 40 °C for 24 h. The obtained gel was transferred to a Teflon-lined autoclave, aged at 100 °C for 24 h, then filtered, and washed with DI water. Subsequently, the sample was dried at 100 °C for 24 h and calcined at 550 °C for 6 h; a heating rate of 2 °C/min was used. The final solid product was mashed to a size range of 53−106 μm.

4.3. Specific Surface Area and Pore Size Distribution Determination. The specific surface area and pore size distribution of highly porous silica were characterized by N_2 physisorption using an Autosorb-1-C (Quantachrome Instruments, Boynton Beach, FL) employing BET and BJH methods at −196 °C. The sample was degassed at 200 °C.[26]

4.4. X-ray Diffraction Analysis. The crystalline structure of a sample was characterized by an X-ray diffractometer (Bruker AXS GmbH, D8 advance, Karlsruhe, Germany). Each XRD pattern was determined using Cu Kα radiation (λ = 1.5406 Å) at 40 kV and 40 mA at a scan rate of 0.02°/0.5 s, a spatial resolution of 75 μm, a slit width of 1 mm, a small angle in the 2θ range of 0−10°, and a wide range of 5−80°.[20] The d-spacing (d) was calculated using Braggs's equation

$$d = \frac{n\lambda}{2\sin\theta} \quad (1)$$

where λ is the X-ray wavelength, θ is the angle of diffraction (rad), and n is the order of the peak plane, which is equal to unity (first-order diffraction).

4.5. Morphological Analysis. The morphology of a sample was analyzed using a field emission scanning electron microscope (JEOL, JSM-7610F, Tokyo, Japan). The sample was coated with platinum (Pt) at 1.00 kV and magnified at 15,000×.[11]

4.6. Fourier Transform Infrared Spectroscopy. Functional groups of a sample were identified via the use of an FTIR spectrometer (Perkin Elmer, Spectrum One, Shelton, CT) within an infrared range of 4000−400 cm^{-1}.[11]

4.7. Temperature-Programmed Desorption Using Ammonia as a Probe Molecule (NH_3-TPD).[33] Experiments were conducted using a TPDRO apparatus (Thermo Scientific, TPDRO 1100, Waltham, MA) to investigate the acidic property of porous silica. 0.2 g of a sample was pretreated by passing He (30 mL/min) at a heating rate of 10 °C/min until 400 °C was reached; such a temperature was maintained for 60 min. The sample was then cooled to 100 °C. Subsequently, 10% v/v NH_3 (using He as a balance gas) was introduced to the sample for 1 h at a flow rate of 30 mL/min. The flow of NH_3 was then disconnected and the sample was flushed with He at a flow rate of 30 mL/min for 1 h to remove the physisorbed NH_3. NH_3 desorption analysis was carried out by flowing He (30 mL/min) and heating the sample at a rate of 10 °C/min from 100 to 600 °C. The intensity of the acid sites

https://doi.org/10.1021/acsomega.2c08299
ACS Omega 2023, 8, 19320−19328

was determined by measuring the weight loss resulting from the desorption of NH_3.

4.8. ζ Potential Determination.[39] ζ Potential determination was conducted using a Zetasizer Nano ZSP (Malvern Instruments, Worcestershire, U.K.). ζ Potential was determined at pH 2.5 and 6.5, which corresponded to the conditions in the gastric and intestinal phases of in vitro digestion, respectively.

4.9. Aflatoxin B1 (AFB1) Adsorption. *4.9.1. Preparation of Standards.* AFB1 standards were prepared as described by Sungsinchai et al.[40] at concentrations of 0, 0.875, 1.75, and 3.5 μg/mL.

4.9.2. Preparation of Artificial Gastric and Intestinal Juices. Artificial gastric juice (AGJ) and artificial intestinal juice (AIJ) were prepared as described by Tso et al.[35] with some modifications. 1 g of NaCl and 1.6 g of pepsin were initially dissolved in sufficient DI water. After that, 36.5% HCl (2.5 mL) was added; the mixture was diluted to 500 mL using DI water to obtain AGJ. The pH of AGJ was adjusted to 2.5 using 0.1 M NaOH. 3.4 g of KH_2PO_4 was dissolved in 250 mL of DI water and the pH of the resulting solution was adjusted to 6.8 using 0.1 M NaOH. Then, 5 g of trypsin was dissolved in DI water and mixed with the KH_2PO_4 solution. 1.5 g of porcine bile salt was added to the solution and diluted to 500 mL using DI water to obtain AIJ. The pH of AIJ was adjusted to 6.5 using 0.1 M NaOH and 36.5% HCl. Both AGJ and AIJ were kept at 4 °C for further use.

4.9.3. In Vitro Digestion and Chromatographic Conditions of AFB1. In vitro digestion was conducted as suggested by Tso et al.[35] with some modifications. 1 mL of AFB1 solution (3.5 μg/mL) was added to 21 mL of AGJ; 3.5 mg of each porous silica was then added. The mixture was incubated in a shaking water bath at 40 °C at 150 rpm for 0, 1, 3, and 5 h. After 5 h, 20 mL of AIJ was added to the mixture; incubation continued in the same shaking water bath at 40 °C at 150 rpm for 0.5, 1, 1.5, and 2 h. After incubation, the mixture was collected and filtered using Whatman paper No. 3. The clean-up and HPLC of the extract were carried out according to the methods of Sungsinchai et al.[40]

Adsorption kinetic equations were used to analyze the adsorption kinetic data.[41] The adsorption capability is given by eq 2.

$$\text{adsorption}\ (\%) = \frac{(C_0 - C_t)}{C_0} \times 100 \quad (2)$$

where C_o is the initial concentration of AFB1 (μg/mL) and C_t is the concentration of AFB1 at the final stage of in vitro digestion (μg/mL).

The pseudo-first-order equation is given in eq 3.

$$\ln\ (q_e - q_t) = \ln\ q_e - k_a t \quad (3)$$

where q_e is the concentration of AFB1 adsorbed at equilibrium (mg/g), q_t is the concentration adsorbed at time t (mg/g), and k_a is the first-order rate constant (h^{-1}). The values of R^2, k_a, and q_e were calculated using a plot of ln $(q_e - q_t)$ versus time.

AUTHOR INFORMATION

Corresponding Author

Chalida Niamnuy − *Department of Chemical Engineering, Faculty of Engineering, Kasetsart University, Bangkok 10900, Thailand; Center for Advanced Studies in Nanotechnology and Its Applications in Chemical, Food and Agricultural Industries, Kasetsart University, Bangkok 10900, Thailand;* orcid.org/0000-0003-2932-2022; Phone: +66 2 797 0999; Email: fengcdni@ku.ac.th; Fax: +66 2 561 4621

Authors

Sirada Sungsinchai − *Department of Chemical Engineering, Faculty of Engineering, Kasetsart University, Bangkok 10900, Thailand*

Sakamon Devahastin − *Advanced Food Processing Research Laboratory, Department of Food Engineering, Faculty of Engineering, King Mongkut's University of Technology Thonburi, Bangkok 10140, Thailand; The Academy of Science, The Royal Society of Thailand, Bangkok 10300, Thailand;* orcid.org/0000-0001-9582-1554

Xiao Dong Chen − *School of Chemical and Environmental Engineering, College of Chemistry, Chemical Engineering and Materials Science, Soochow University, Suzhou, Jiangsu 215123, P. R. China*

Metta Chareonpanich − *Department of Chemical Engineering, Faculty of Engineering, Kasetsart University, Bangkok 10900, Thailand; Center for Advanced Studies in Nanotechnology and Its Applications in Chemical, Food and Agricultural Industries, Kasetsart University, Bangkok 10900, Thailand;* orcid.org/0000-0002-4333-337X

Complete contact information is available at: https://pubs.acs.org/10.1021/acsomega.2c08299

Notes

The authors declare no competing financial interest.

ACKNOWLEDGMENTS

This work was financially supported by the Kasetsart University Research and Development Institute (KURDI) and the Office of the Ministry of Higher Education, Science, Research and Innovation as well as the Thailand Science Research and Innovation through the Kasetsart University Reinventing University Program 2021. The work was also supported by the National Science and Technology Development Agency (NSTDA) through the Chair Professor Grant (Grant No. P-20-52263).

REFERENCES

(1) Oliveira, J. A.; Cunha, F. A.; Ruotolo, L. A. Synthesis of zeolite from sugarcane bagasse fly ash and its application as a low-cost adsorbent to remove heavy metals. *J. Cleaner Prod.* **2019**, *229*, 956−963.

(2) Abo-El-Enein, S. A.; Eissa, M. A.; Diafullah, A. A.; Rizk, M. A.; Mohamed, F. M. Removal of some heavy metals ions from wastewater by copolymer of iron and aluminum impregnated with active silica derived from rice husk ash. *J. Hazard. Mater.* **2009**, *172*, 574−579.

(3) Chandrasekar, G.; Ahn, W. S. Synthesis of cubic mesoporous silica and carbon using fly ash. *J. Non-Cryst. Solids* **2008**, *354*, 4027−4030.

(4) Batra, V. S.; Urbonaite, S.; Svensson, G. Characterization of unburned carbon in bagasse fly ash. *Fuel* **2008**, *87*, 2972−2976.

(5) Siregar, A. G. A.; Manurung, R.; Taslim, T. Synthesis and characterization of sodium silicate produced from corncobs as a heterogeneous catalyst in biodiesel production. *Indones. J. Chem.* **2021**, *21*, 88−96.

(6) Awuchi, C. G.; Ondari, E. N.; Nwozo, S.; Odongo, G. A.; Eseoghene, I. J.; Twinomuhwezi, H.; Ogbonna, C. U.; Upadhyay, A. K.; Adeleye, A. O.; Okpala, C. O. R. Mycotoxins' toxicological mechanisms involving humans, livestock and their associated health concerns: A review. *Toxins* **2022**, *14*, 167.

(7) Vekiru, E.; Fruhauf, S.; Rodrigues, I.; Ottner, F.; Krska, R.; Schatzmayr, G.; Ledoux, D. R.; Rottinghaus, G.; Bermudez, A. J. *In vitro* binding assessment and in vivo efficacy of several adsorbents against aflatoxin B1. *World Mycotoxin J.* **2015**, *8*, 477−488.
(8) Saramas, D.; Ekgasit, S. Nano-zinc oxide-doped activated carbon from popped rice and its application for feed additive. *Eng. J.* **2021**, *25*, 41−50.
(9) Nešić, K.; Jakšić, S.; Popov, N.; Živkov-Baloš, M.; Pajić, M.; Zloh, B.; Polaček, V. *In vitro* assessment of binding capability of combined adsorbent (bentonite with yeast cell wall extracts) and aflatoxin B1. *Arch. Vet. Med.* **2020**, *13*, 41−52.
(10) Zavala-Franco, A.; Hernández-Patlán, D.; Solís-Cruz, B.; López-Arellano, R.; Tellez-Isaias, G.; Vázquez-Durán, A.; Méndez-Albores, A. Assessing the aflatoxin B1 adsorption capability between biosorbents using an in vitro multicompartmental model simulating the dynamic conditions in the gastrointestinal tract of poultry. *Toxins* **2018**, *10*, 484.
(11) Ruengrung, P.; Niamlaem, M.; Jongkraivut, P.; Donphai, W.; Chareonpanich, M. Synthesis of bagasse ash-derived silica-aluminosilicate composites for methanol adsorption. *Mat.Today: Proceed.* **2020**, *23*, 726−731.
(12) Kersting, M.; Olejnik, M.; Rosenkranz, N.; Loza, K.; Breisch, M.; Rostek, A.; Westphal, G.; Bünger, J.; Ziegler, N.; Ludwig, A.; Köller, M.; Sengstock, C.; Epple, M. Subtoxic cell responses to silica particles with different size and shape. *Sci. Rep.* **2020**, *10*, No. 21591.
(13) Li, Y. N.; Wang, R.; Luo, X.; Chen, Z.; Wang, L.; Zhou, Y.; Liu, W.; Cheng, M.; Zhang, C. Synthesis of rice husk-based MCM-41 for removal of aflatoxin B1 from peanut oil. *Toxins* **2022**, *14*, No. 87.
(14) Pellicer-Castell, E.; Belenguer-Sapiña, C.; Borràs, V. J.; Amorós, P.; El Haskouri, J.; Herrero-Martínez, J. M.; Mauri-Aucejo, A. R. Extraction of aflatoxins by using mesoporous silica (type UVM-7), and their quantitation by HPLC-MS. *Microchim. Acta* **2019**, *186*, No. 792.
(15) Prapapanpong, J.; Udomkusonsri, P.; Mahavorasirikul, W.; Choochuay, S.; Tansakul, N. *In vitro* studies on gastrointestinal monogastric and avian models to evaluate the binding efficacy of mycotoxin adsorbents by liquid chromatography-tandem mass spectrometry. *J. Adv. Vet. Anim. Res.* **2019**, *6*, 125−132.
(16) Kolawole, O.; Meneely, J.; Greer, B.; Chevallier, O.; Jones, D. S.; Connolly, L.; Elliott, C. Comparative *in vitro* assessment of a range of commercial feed additives with multiple mycotoxin binding claims. *Toxins* **2019**, *11*, 659.
(17) Avantaggiato, G.; Havenaar, R.; Visconti, A. Assessment of the multi-mycotoxin-binding efficacy of a carbon/aluminosilicate-based product in an *in vitro* gastrointestinal model. *J. Agric. Food Chem.* **2007**, *55*, 4810−4819.
(18) Pellicer-Castell, E.; Belenguer-Sapiña, C.; Amoros, P.; Herrero-Martínez, J. M.; Mauri-Aucejo, A. R. Bimodal porous silica nanomaterials as sorbents for an efficient and inexpensive determination of aflatoxin M1 in milk and dairy products. *Food Chem.* **2020**, *333*, No. 127421.
(19) Bardestani, R.; Patience, G. S.; Kaliaguine, S. Experimental methods in chemical engineering: Specific surface area and pore size distribution measurements-BET, BJH, and DFT. *Can. J. Chem. Eng.* **2019**, *97*, 2781−2791.
(20) Tanggarnjanavalukul, C.; Donphai, W.; Witoon, T.; Chareonpanich, M.; Limtrakul, J. Deactivation of nickel catalysts in methane cracking reaction: Effect of bimodal meso−macropore structure of silica support. *Chem. Eng. J.* **2015**, *262*, 364−371.
(21) Essomba, J. S.; Alla, J. P.; Belibi, P. D. B.; Fathima, N. N. Clay/polymer nanocomposite material: a sustainable approach of leather industries wastewater treatment. *Int. J. Environ. Sci. Technol.* **2022**, *19*, 5181−5194.
(22) Witoon, T.; Chareonpanich, M.; Limtrakul, J. Synthesis of bimodal porous silica from rice husk ash via sol−gel process using chitosan as template. *Mater. Lett.* **2008**, *62*, 1476−1479.
(23) Hessien, M.; Prouzet, E. Synthesis of hierarchical porous silica by sol-gel of sodium silicate and nanoemulsion templating: Effective combination conditions. *ChemistrySelect* **2021**, *6*, 1440−1447.
(24) Aziz, M. A. H.; Jalil, A. A.; Rahman, A. F. A.; Fatah, N. A. A.; Izan, S. M.; Hussain, I.; Hambali, H. U. Toluene side chain alkylation with methanol over silica catalyst. *IOP Conf. Series: Mater. Sci. Eng.* **2020**, *808*, No. 012004.
(25) Kiatphuengporn, S.; Chareonpanich, M.; Limtrakul, J. Effect of unimodal and bimodal MCM-41 mesoporous silica supports on activity of Fe−Cu catalysts for CO_2 hydrogenation. *Chem. Eng. J.* **2014**, *240*, 527−533.
(26) Panchan, N.; Donphai, W.; Junsomboon, J.; Niamnuy, C.; Chareonpanich, M. Influence of the calcination technique of silica on the properties and performance of Ni/SiO_2 catalysts for synthesis of hydrogen via methane cracking reaction. *ACS Omega* **2019**, *4*, 18076−18086.
(27) Ogunmodede, O. T.; Ojo, A. A.; Adewole, E.; Adebayo, O. L. Adsorptive removal of anionic dye from aqueous solutions by mixture of kaolin and bentonite clay: Characteristics, isotherm, kinetic and thermodynamic studies. *Iran. J. Energy Environ.* **2015**, *6*, 147−153.
(28) Li, J.; Wu, W.; Yang, H.; Wang, X.; Wang, X.; Sun, C.; Hu, Z. Rigid silica xerogel/alumina fiber composites and their thermal insulation properties. *J. Porous Mater.* **2019**, *26*, 1177−1184.
(29) Nhavene, E. P. F.; Andrade, G. F.; Faria, J. A. Q. A.; Gomes, D. A.; de Sousa, E. M. B. Biodegradable Polymers Grafted onto Multifunctional Mesoporous Silica Nanoparticles for Gene Delivery. *ChemEng.* **2018**, *2*, No. 24.
(30) Watthanachai, C.; Ngamcharussrivichai, C.; Pengprecha, S. Synthesis and characterization of bimodal mesoporous silica derived from rice husk ash. *Eng. J.* **2019**, *23*, 25−34.
(31) Thakur, S.; Verma, A.; Raizada, P.; Gunduz, O.; Janas, D.; Alsanie, W. F.; Scarpa, F.; Thakur, V. K. Bentonite-based sodium alginate/dextrin cross-linked poly (acrylic acid) hydrogel nanohybrids for facile removal of paraquat herbicide from aqueous solutions. *Chemosp.* **2022**, *291*, No. 133002.
(32) Zaitan, H.; Bianchi, D.; Achak, O.; Chafik, T. A comparative study of the adsorption and desorption of o-xylene onto bentonite clay and alumina. *J. Hazard. Mater.* **2008**, *153*, 852−859.
(33) Niamnuy, C.; Prapaitrakul, P.; Panchan, N.; Seubsai, A.; Witoon, T.; Devahastin, S.; Chareonpanich, M. Synthesis of dimethyl ether via CO_2 hydrogenation: Effect of the drying technique of alumina on properties and performance of alumina-supported copper catalysts. *ACS Omega* **2020**, *5*, 2334−2344.
(34) Aljlil, S. A. Fabrication of bentonite−silica sand/suspended waste palm leaf composite membrane for water purification. *Membranes* **2020**, *10*, No. 290.
(35) Tso, K. H.; Ju, J. C.; Fan, Y. K.; Chiang, H. I. Enzyme degradation reagents effectively remove mycotoxins deoxynivalenol and zearalenone from pig and poultry artificial digestive juices. *Toxins* **2019**, *11*, No. 599.
(36) Abbasi Pirouz, A.; Selamat, J.; Sukor, R. Noorahya Jambari, N. Effective detoxification of aflatoxin B1 and ochratoxin a using magnetic graphene oxide nanocomposite: Isotherm and kinetic study. *Coatings* **2021**, *11*, No. 1346.
(37) Zhang, W.; Zhang, S.; Wang, J.; Dong, J.; Cheng, B.; Xu, L.; Shan, A. A novel adsorbent albite modified with cetylpyridinium chloride for efficient removal of zearalenone. *Toxins* **2019**, *11*, 674.
(38) Li, Y.; Wang, R.; Chen, Z.; Zhao, X.; Luo, X.; Wang, L.; Li, Y.; Teng, F. Preparation of magnetic mesoporous silica from rice husk for aflatoxin B1 removal: Optimum process and adsorption mechanism. *PLoS One* **2020**, *15*, No. e0238837.
(39) Zhai, X.; Guo, J.; Zhang, W.; Yang, D. A. Effect of zeta potential on coating morphology of SiO_2-coated copper powder and conductivity of copper film. *Chem. Pap.* **2020**, *74*, 2123−2131.
(40) Sungsinchai, S.; Niamnuy, C.; Jaree, A.; Devahastin, S. Influences of pretreatment and drying methods on composition, micro/molecular structures and some health-related functional characteristics of dietary fibre powder from orange pulp residues. *Int. J. Food Sci. Technol.* **2017**, *52*, 2217−2229.
(41) Zahoor, M.; Khan, F. A. Adsorption of aflatoxin B1 on magnetic carbon nanocomposites prepared from bagasse. *Arabian J. Chem.* **2018**, *11*, 729−738.

https://doi.org/10.1021/acsomega.2c08299
ACS Omega 2023, 8, 19320−19328